

# Flow in linearly sheared two dimensional foams: from bubble to bulk scale

Gijs Katgert, Andrzej Latka, Matthias E. Möbius, and Martin van Hecke

*Kamerlingh Onnes Lab, Universiteit Leiden, Postbus 9504, 2300 RA Leiden, The Netherlands*

(Dated: October 25, 2018)

We probe the flow of two dimensional foams, consisting of a monolayer of bubbles sandwiched between a liquid bath and glass plate, as a function of driving rate, packing fraction and degree of disorder. First, we find that bidisperse, disordered foams exhibit strongly rate dependent and inhomogeneous (shear banded) velocity profiles, while monodisperse, ordered foams are also shear banded, but essentially rate independent. Second, we introduce a simple model based on balancing the averaged drag forces between the bubbles and the top plate,  $\bar{F}_{bw}$  and the averaged bubble-bubble drag forces  $\bar{F}_{bb}$ , and assume that  $\bar{F}_{bw} \sim v^{2/3}$  and  $\bar{F}_{bb} \sim (\partial_y v)^\beta$ , where  $v$  and  $(\partial_y v)$  denote average bubble velocities and gradients. This model captures the observed rate dependent flows for  $\beta \approx 0.36$ , and the rate independent flows for  $\beta \approx 0.67$ . Third, we perform independent rheological measurements of  $\bar{F}_{bw}$  and  $\bar{F}_{bb}$ , both for ordered and disordered systems, and find these to be fully consistent with the forms assumed in the simple model. Disorder thus modifies the exponent  $\beta$ . Fourth, we vary the packing fraction  $\phi$  of the foam over a substantial range, and find that the flow profiles become increasingly shear banded when the foam is made wetter. Surprisingly, our model describes flow profiles and rate dependence over the whole range of packing fractions with the same power law exponents — only a dimensionless number  $k$  which measures the ratio of the pre-factors of the viscous drag laws is seen to vary with packing fraction. We find that  $k \sim (\phi - \phi_c)^{-1}$ , where  $\phi_c \approx 0.84$ , corresponding to the 2d jamming density, and suggest that this scaling follows from the geometry of the deformed facets between bubbles in contact. Overall, our work shows that the presence of disorder qualitatively changes the effective bubble-bubble drag forces, and suggests a route to rationalize aspects of the ubiquitous Herschel-Bulkley (power law) rheology observed in a wide range of disordered materials.

PACS numbers: 47.15.gm, 47.57.Bc, 83.50.Lh

## I. INTRODUCTION

Foams, which are dispersions of densely packed gas bubbles in a liquid, exhibit an intricate mix of elastic, plastic and viscous behavior reminiscent of the mechanics of other disordered materials such as colloidal suspensions, granular media and emulsions [1, 2, 3, 4, 5, 6]. When left unperturbed, foams jam into a meta-stable state where surface tension provides the restoring force underlying their elastic response for small strains [1, 4, 7]. Under continuous driving the foam starts to flow, and the viscous dissipation that arises in the thin fluid films that surround the gas bubbles becomes important. Macroscopically, the steady state rheology of foams exhibits shear thinning, and the stress  $\tau$  as function of strain rate  $\dot{\gamma}$  is generally non-linear, often taking a Herschel-Bulkley form:  $\tau = \tau_Y + c_1 \dot{\gamma}^\beta$ , where  $\tau_Y$  denotes the yield stress, and where the viscous stress  $\tau_V \equiv \tau - \tau_Y$  scales nontrivially with the strain rate  $\dot{\gamma}$  [1, 3, 8, 9, 10, 11, 12, 13, 14]. In addition, in many situations, the flow is inhomogeneous and localizes in a shear band [1, 12, 14, 15, 16].

In an earlier Letter [14] we experimentally probed the flow of disordered, bidisperse 2d foams which are trapped between the fluid phase and a top-plate. The 2d nature allows for direct imaging of the bubble dynamics and of the shear banded flow profiles in this system. Combining measurements of the flow profiles with rheological measurements, we established that viscous interactions between neighboring bubbles scale differently with velocity gradients than the effective viscous interactions at

the global scale. We captured the rate-dependent shear banding exhibited by our system in a nonlinear drag force balance model. Here we expand on these findings, discuss new results for the effect of varying the wetness of the foam, and provide extensive additional evidence to support our main conclusions.

To understand the rheology and shear band formation in our system, three ingredients need to be described and combined appropriately: (i) Interactions with the top plate. (ii) Local bubble interactions. (iii) Disorder.

*Top plate* — In recent years, a variety of studies have addressed the formation of shear bands in (quasi) two-dimensional foams, consisting of a single layer of macroscopic bubbles. Such single layers can be made by freely floating the bubbles on the surface of a surfactant solution ("bubble raft") [12, 17, 18], by trapping them between a top glass plate and the surfactant solution ("liquid-glass") [14, 18, 19, 20, 21], or by trapping them between two parallel glass plates (Hele-Shaw cell) [15].

In a seminal paper by Debrégeas et al. [15], a bidisperse foam in Hele-Shaw Couette cell was sheared and narrow shear banded flow profiles were obtained [15]. While initially it was believed that for slow flows, the effect of the viscous drag forces exerted by the confining glass plates would be negligible [1, 22], these drag forces have turned out to be crucial. First, Couette experiments in bubble rafts found completely smooth flow behavior [12]. Second, in experiments where a monodisperse foam was linearly sheared with and without confining glass plate on top [18], one observes smooth velocity

profiles for the bubble raft but highly shear banded flows for the liquid-glass geometry. The precise connection between the drag forces due to the confining plates and the occurrence of shear banding in confined foams is still a subject of debate [22, 23].

A simple continuum model that balances the top plate drags and the inter-bubble drags (modeled with a Bingham constitutive relation) captures both the rate independence and exponentially localized shear bands seen in the linear liquid-glass cell [14, 24] — here we will build on and extend this model to capture the experimentally observed nonlinear, rate dependent rheology of disordered foams.

*Local interactions* — At the microscopic level, bubble interactions are a combination of elastic repulsion, typically harmonic for small deformations [25, 26, 27, 28], and nonlinear viscous drag forces [13, 14, 29, 30, 31, 32, 33]. Such drag forces arise when two bubbles slide past each other or when a bubble slides past a solid boundary. The viscous drag forces originate in the thin films that surround foam bubbles, and have recently received renewed attention [13, 29, 30, 31, 32, 33]. Already for a single bubble sliding past a solid wall, Bretherton showed that the drag force scales nonlinearly with the bubble velocity [13, 32, 34], and by analogy one would expect the drag forces arising between sliding bubbles to be nonlinear also — indeed Denkov et al. recently suggested that a similar scaling applies to the viscous drag force between bubbles [33].

Here we measure these drag forces directly by rheological experiments where two rows of ordered bubbles are sheared past each other.

*Disorder* — Foam flows are disordered and intermittent at the multi-bubble scale [5, 7, 13, 14, 24, 35, 36]. For such disordered systems, the affine approach, where one simply scales up local elastic or viscous interactions, often fails to describe the macroscopic behavior — this is by now well established for shear deformations in granular and foam-like systems [37, 38, 39], and a similar picture is emerging from simulations of the flow of viscous particles [35, 40, 41, 42, 43]. In the present work we present strong experimental evidence for the failure of the affine approach to describe drag forces in flowing systems.

### Outline

In this paper, we describe an experiment in which we have linearly sheared a 2d foam and we disentangle the roles of the top plate, the local bubble interactions and the disorder, as well as the role of the wetness of the foam.

In section II we describe our experimental setup. In section III we present experimental results for flow profiles for a range of strain rates and span-wise widths of our system. We find that the flow depends crucially on the applied strain rate  $\dot{\gamma}_a$ : disordered, bidisperse foams ex-

hibit rate dependent flow profiles, which become increasingly shear-banded for large  $\dot{\gamma}_a$ . We capture our findings in a model in which the time-averaged drag forces between bubble and top plate,  $\overline{F}_{bw}$ , and between neighboring bubbles,  $\overline{F}_{bb}$  are balanced. While the continuum limit of our model is similar in spirit to [24], the crucial new ingredient is nonlinear scaling laws for the wall drag and the bulk stress — these nonlinear scalings are essential for capturing the observed rate dependence.

In section IV, we probe the scaling of the drag forces by independent rheological measurements, allowing us to directly probe the role of disorder by comparing the rheology of small ordered and larger disordered bubble rafts. We find the averaged drag forces in the disordered foam to scale *differently* from the local drag forces between individual bubbles, which we have measured at high resolution and analyze in a novel way.

In contrast, for monodisperse, ordered foams the local, averaged and top-plate drag forces all scale similarly, causing rate-independent flows similar to those seen by Wang et al. [18], and we discuss these in section V.

In section VI we further probe the connection between the viscous drag forces at the bubble scale and the bulk viscous forces by performing additional linear shear experiments over a range of packing (air) fractions  $\phi$ . We find that the contribution of averaged bubble-bubble drag forces vanishes algebraically as  $\phi - \phi_c$ , when the packing fraction is decreased towards a critical value  $\phi_c$ , which we identify with the (un)jamming density —  $\phi_c \approx 0.84$ . We relate the vanishing of the averaged bubble-bubble drag forces at  $\phi_c$  to the vanishing overlap between bubbles at unjamming.

The simple elastic interaction (typically harmonic for small deformations [25, 26, 27, 28]) and the absence of solid friction make static packings of foam bubbles eminently suited to compare to simulations of the popular soft frictionless sphere model [38, 44, 45]. Our work illustrates the great potential of foams to elucidate the *flow* behavior of simple systems near jamming [40, 41, 42, 43].

## II. EXPERIMENTAL DETAILS

In this section we describe in detail a novel experimental setup to induce linear shear flow in two-dimensional foams. We also detail the analysis techniques used to extract velocity profiles, and discuss measurements which show that coarsening and fluid drag can be neglected.

### A. Setup

We create foam bubbles on the surface of a reservoir of soapy solution (of depth 3.5 cm), consisting of 80% by volume demineralized water, 15% glycerol and 5% Blue Dawn dishwashing agent (Proctor & Gamble), by bubbling nitrogen through the solution via syringe needles of variable aperture. We measure the bath surface tension

$\sigma$  with the pendant drop method [46] and find  $\sigma = 28 \pm 1$  mN/m. We measure the dynamic viscosity  $\eta$  with a Cannon Ubbelohde viscometer and find  $\eta = 1.8 \pm 0.1$  mPa.s.

Fig. 1 shows our experimental setup: the bubbles are contained inside an aluminum frame (400x230 mm) which is leveled with the liquid surface and which supports glass top plates to which the bubbles bridge once they are in place. The top plates consist of three adjacent glass plates with slits to accommodate two PMMA wheels of radius 195 mm and thickness 9.5 mm which drive the flow. The vertical gap between the liquid surface and the glass plates can be varied to control the packing fraction of bubbles  $\phi$ .

The wheels, which are grooved to provide a no-slip boundary for the bubbles, can be lowered into and raised out of the bath through the slits. The wheels are connected to two Lin Engineering stepper motors, each driven by micro-stepping driver, and are rotated in opposite directions. At any point along the line where the wheels contact the foam bubbles the horizontal component of the driving velocity is a constant (see Fig. 1b).

We obtain our data from the central 60 mm of the shearing region — marked by the horizontal lines in Fig. 1(a)— to avoid effects caused by the recirculation of the foam at the edges of the wheels. In this central part no motion is observed due to the vertical component of the radial velocity. At the edges of the slits, bubbles do leave the system, while being pinned to the wheels. This does not result in holes in the foam layer, either because at high driving velocities the bubbles reenter the system before rupturing while traveling on the wheel, or because at low velocities bubbles from outside the shearing region are pushed inwards due to the bubble surplus at the edges. The resulting driving velocity gives rise to a global strain rate  $\dot{\gamma} = 2v_0/W$ , where  $W$  denotes the gap between the wheels, which we vary between 5 and 10 cm.

## B. Imaging and Analysis

We wish to characterize the average flow in the  $x$ -direction as a function of the span-wise coordinate  $y$ . The average velocity profiles are obtained from a series of images which we record with an 8 bit Foculus BW 432 CCD camera (1280x1024 pixels) equipped with a Tamron 28-300 telezoom objective. In the images, 1 pixel corresponds to approximately 0.1 mm. To optimize the brightness and obtain images in which the bubbles appear as circles, the foam is lit laterally by two fluorescent tubes, each driven by high frequency ballasts to prevent flickering in the images. The bottom of the reservoir is covered with a black plate to improve contrast. Typical images are shown in Fig. 2.

The frame rate is fixed such that the displacement at the wheels is fixed at 0.15 mm between frames. Since the flow is strongly intermittent, with large fluctuations

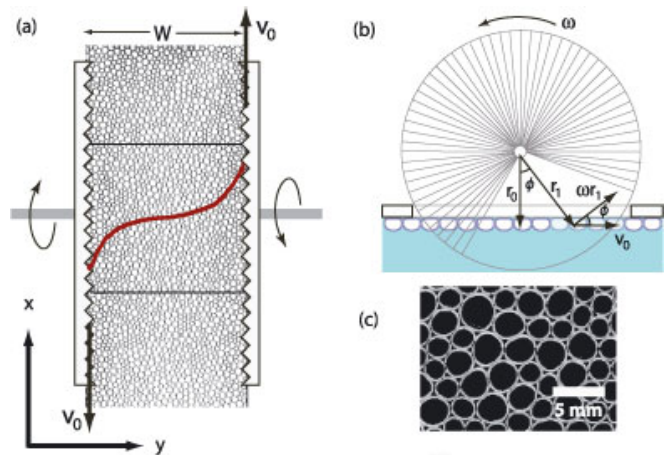


FIG. 1: (Color online) (a) Schematic topview of the experimental setup.  $W$  represents the gap width and the two horizontal lines indicate the edge of the region over which the velocity profiles are calculated. The red curve depicts one such profile. (b) Sideview of the shearing wheels. The slits in the glass plate are drawn for clarity. That the in-plane component of the motion of the boundary is constant can be seen as follows: by trivial geometry, we obtain that  $v_0 = \omega r_1 \cos \phi$ , but since  $r_1 = \frac{r_0}{\cos \phi}$ , at any point along the contact line of 230 mm, the layer of bubbles is sheared with a driving velocity  $v_0 = \omega \frac{r_0}{\cos \phi} \cos \phi = \omega r_0$ . (c) Experimental image of part of the foam, the scalebar represents 5 mm.

in the bubble displacements, we take 1000 frames per run, corresponding to a strain of 4 for a 5 cm gap, as we are interested in averaged velocity profiles. We pre-shear the system before taking data, so that a steady state is reached.

We obtain the velocity profiles both through particle tracking and a Particle Image Velocimetry-like technique, where for each  $y$ -value, we calculate the cross-correlation  $(C_n)^2$  between the corresponding image line in the  $P_n(x)$  of length  $m$  and the same image line  $P_{n+1}(x)$  in the next frame shifted by an amount  $\tau$ :

$$(C_n(\tau))^2 = \sum_{i=0}^{m-\tau} P_n(i)P_{n+1}(i + \tau). \quad (1)$$

We can then proceed in two ways. The first method is to add up all cross-correlations from all frames for each  $y$ -value, and calculate the average displacement  $\Delta x$  per frame by fitting a parabola  $p_n(\tau)$  to the resulting sum of cross-correlations and taking the peak value of that parabola:

$$\Delta x(y) = \max \left( \sum_{n=0}^{999} p_n(\tau) \right). \quad (2)$$

In the second method we fit a parabola to each cross-correlation separately and obtain the average displacement by averaging the maxima of all individual parabolas:

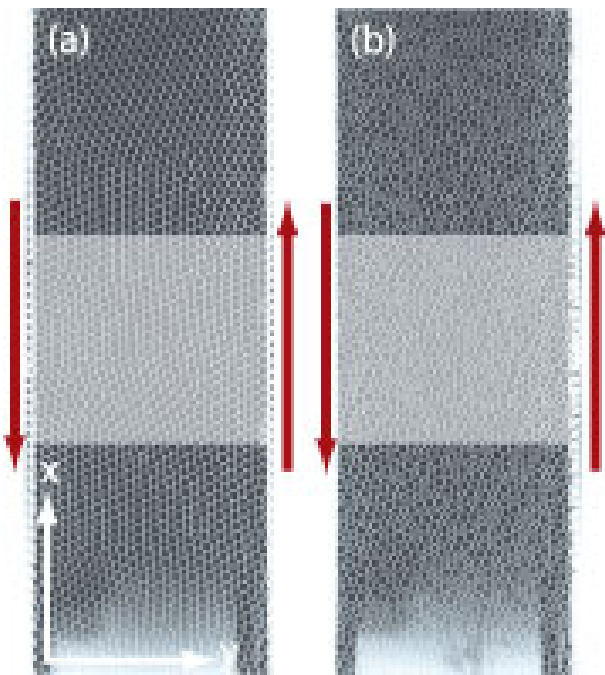


FIG. 2: (Color online) Images of sheared regions for both (a) monodisperse and (b) bidisperse foams. Shear is indicated by the arrows. The highlighted area is where data analysis is performed on.

las:

$$\Delta x(y) = \langle \max(p_n(\tau)) \rangle. \quad (3)$$

By comparing to average velocity profiles obtained by particle tracking [36], we find that the latter procedure gives the closest match to the tracking velocity profiles, and we have employed this procedure throughout. We thus obtain both spatially (in the  $x$ -direction) and temporally averaged velocity profiles. Despite the intermittent character of the flow, we obtain smooth reproducible velocity profiles.

### C. Coarsening and fluid drag

To characterize the amount of coarsening we measure the bubble size distribution by measuring the surface area of the bubbles in the images. We obtain well defined size distributions which show little coarsening over the duration of the runs, which corresponds to about 2 hours (Fig. 3a).

We have checked that the drag on the foam bubbles due to flow of the bulk liquid underneath is negligible by measuring the velocity profile of bubbles floating on a very shallow layer of bulk fluid. In this case the fluid surface velocity is decreased due to the no-slip boundary condition at the reservoirs' bottom. We do not, within experimental uncertainty, observe a change in the experimental velocity profiles in this geometry.

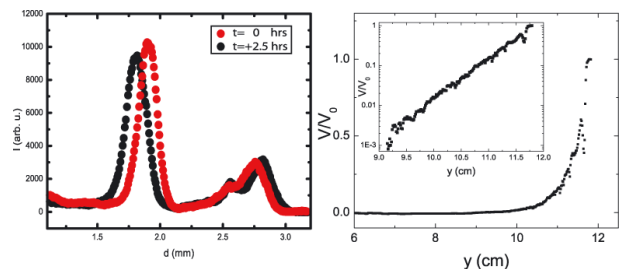


FIG. 3: (a) Size distribution and coarsening over the duration of an experimental run for bidisperse foams. (b) Flow at the liquid surface in the absence of bubbles, as imaged by depositing silver powder. Inset: same profile on lin-log scale, showing exponential decay away from the boundaries.

We furthermore measure the velocity profile of the liquid surface itself at the same fluid level as in the foam experiments by imaging the flow of silver particles that were sprinkled on the liquid surface, see Fig. 3b. We observe a steeply decreasing velocity profile at the fluid surface, which implies that even if the fluid drag were of the order of the other drags acting on the bubbles, it would not significantly alter the flow profiles except near the wheels.

We thus conclude that the bubble size distribution is essentially constant during an experimental time frame, and that the dominant drag forces are those between bubbles and top plate, and those between contacting bubbles.

## III. LINEAR SHEAR OF TWO DIMENSIONAL FOAMS

In this section we explore the rate dependent shear flows in our system experimentally. By fitting our experimental data to a nonlinear drag force balance model, we deduce the dependence of the averaged bubble-bubble and bubble-wall drag forces as function of the local strain rate and velocity.

### A. Flow of disordered foams

We measure averaged velocity profiles in disordered twodimensional foams. These foams are produced by bubbling a fixed flow rate of nitrogen through syringe needles of 2 different inner diameters, such that bubbles of  $1.8 \pm 0.1$  and  $2.7 \pm 0.2$  mm result (at 59-41 number ratio). The bubbles are gently mixed with a spoon until a disordered monolayer results. For gap widths of 5, 7 and 9 cm, we drive the foam at 6 different velocities, spanning 2.5 decades:  $v_0 = 0.026, 0.083, 0.26, 0.83, 2.6$  and  $8.3$  mm/s.

Note that we perform the sweep in driving velocities from fast to slow and that we pre-shear the system for one full wheel rotation, to start with bubbles covering

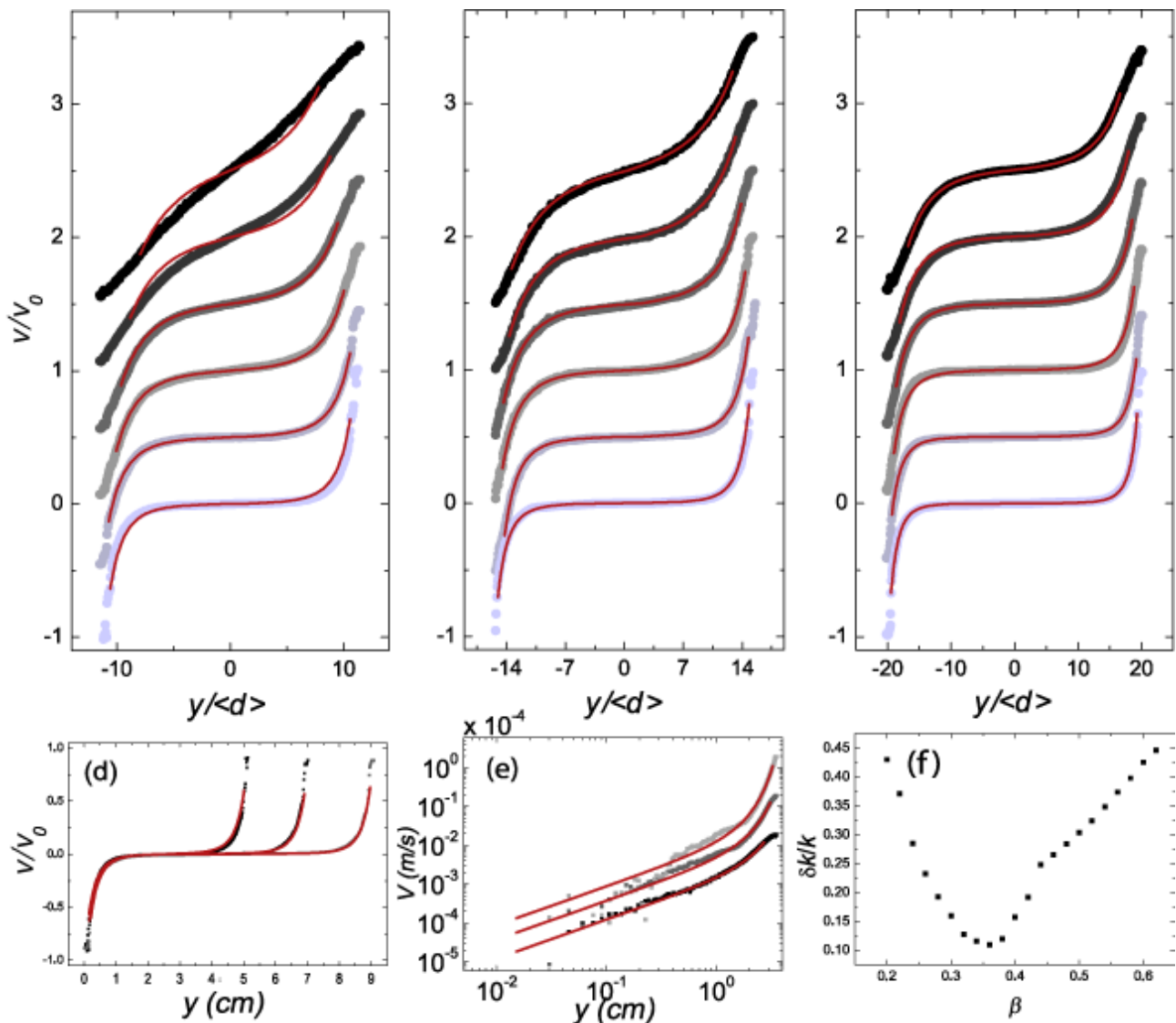


FIG. 4: (Color online) (a-c) Flow profiles for a gap width  $W = 5$  (a)  $7$  (b) and  $9$  (c) cm. From black to light grey,  $v_0 = 0.026$  mm/s,  $0.083$  mm/s,  $0.26$  mm/s,  $0.83$  mm/s,  $2.6$  mm/s and  $8.3$  mm/s. For all gap widths we observe that the localization near the driving wheels increases for increasing driving velocity. For clarity the profiles are each offset vertically by  $0.5 \times v/v_0$ . Solid red curves: fits to the drag force balance model of section III B. (d) Profiles at  $2.6$  mm/s for all three gap widths. Regardless of the gap width all profiles decay at the same rate. (e) Examples of profiles and fits on a log-log plot, highlighting the linear tails of the profiles.  $v_0 = 0.026, 0.26, 2.6$  mm/s,  $W = 5$  cm. (f) As explained in section III C 1, the minimum in  $\beta$  is found by calculating the variance  $\sqrt{\langle \delta k^2 \rangle} / k^2$  of  $k$  over all 18 profiles depicted in (a-c). The minimum in the variance is seen at  $\beta = 0.36$  — see section III C.

the wheel [47] and ensure that we have reached a steady state. To fix the packing fraction, we fix the gap between glass plate and liquid surface at  $2.25 \pm 0.01$  mm. We have measured (see section VI) that for this gap the packing fraction is  $\phi = 0.965 \pm 0.005$ .

Results are plotted in Fig. 4(a-c): the profiles exhibit shear banding, and for all gap widths the profiles become increasingly shear banded at increasing driving velocities. The slowest runs at  $W = 5$  cm yield essentially linear velocity profiles. We suggest that these shapes are due to the small gap width, which results in overlapping shear

banded profiles resembling a linear profile, and in what follows, we will present a model that supports this conclusion.

In Fig. 4(d) we plot velocity profiles for a driving velocity of  $0.26$  mm/s for all three gap widths together, which clearly show that for all widths, the velocity profiles decay similarly. Fig. 4(d) thus suggests that in this experiment the driving velocity at the edges, instead of the overall shear, sets the velocity profiles, and that the local response to forcing will provide the key towards understanding the shape of these profiles. Note finally that

the profiles do not exhibit significant slip with respect to shearing wheels, except for the fastest runs, where the slip is less than 20 %.

## B. Model

We now propose a model to account for the shear banding behavior discussed above, by considering the balance of the averaged viscous drag forces.

### 1. Drag forces on individual bubbles

The drag force on a single bubble that slides past a solid wall was first investigated by Bretherton [34] and has recently received renewed attention [13, 29, 30, 31, 32, 48]. The crucial finding is that  $F_{bw}$ , the drag force per bubble sliding past a solid wall, scales as

$$F_{bw} = f_{bw}(Ca)^{2/3} = f_{bw}(\eta v/\sigma)^{2/3}, \quad (4)$$

with  $\eta$  the bulk viscosity,  $\sigma$  the surface tension,  $f_{bw}$  a constant with dimensions of force and  $Ca$  the capillary number. Typically  $f_{bw} \propto \sigma r_c$ , with  $r_c$  the radius of the deformed contact between bubble and wall [48]. For bubbles in a soapy solution, the 2/3 scaling with  $Ca$  only holds for surfactants that are mobile [13]. Results from [49] strongly indicate that this is indeed the case for our surfactant Dawn, as we will confirm below.

The drag force between 2 bubbles sliding past each other,  $F_{bb}$ , has not received much attention up to now, although [50] provides indirect evidence that it scales like  $F_{bb} \propto (\eta \Delta Ca)^\zeta$ , with  $\Delta Ca \equiv \eta \Delta v/\sigma$ . In a very recent Letter it is explicitly shown that, for ordered bubble motion  $F_{bb}$  scales indeed as  $(\Delta Ca)^\zeta$  [33]. The authors find  $\zeta = 0.5$ , although various physico-chemical peculiarities, as well as the range of  $Ca$  one measures in, can alter this exponent.

Taking all of this into consideration, it seems reasonable to assume that:

$$F_{bb} = f_{bb}(\eta \Delta v/\sigma)^\zeta. \quad (5)$$

While the dissipation leading to  $F_{bw}$  occurs at the perimeter of the flattened facet [13] — hence the prefactor  $f_{bw} \propto \sigma r_c$  —  $f_{bb}$  scales  $\propto \sigma \kappa_c^2$ , with  $\kappa_c$  the radius of the deformed contact between bubbles, thus reflecting the different physical mechanism behind this scaling [33].

### 2. Stress balance

We divide our shearing region in lanes labeled  $i$  and assume that on every lane the *time-averaged* top plate drag per bubble  $\bar{F}_{bw}^i$  balances with the time-averaged

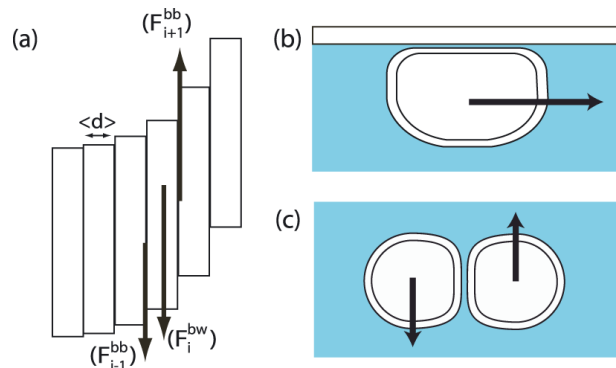


FIG. 5: (Color online) Illustration of drag balance model. The shear region is divided in lanes labeled  $i$  which all experience drag forces due to the top plate and due to both neighboring lanes. (b-c) Illustration of the films around which the viscous drag forces act.

viscous drag per bubble due to the lane to the left ( $\bar{F}_{bb}^i$ ) and right ( $\bar{F}_{bb}^{i+1}$ ), see Fig. 5:

$$\bar{F}_{bb}^{i+1} - \bar{F}_{bw}^i - \bar{F}_{bb}^i = 0. \quad (6)$$

We assume that the averaged drag forces scale similarly to the local drag forces. For the averaged bubble-wall forces we assume:

$$\bar{F}_{bw}^i = f_{bw}(\eta v^i/\sigma)^{2/3}, \quad (7)$$

while for the averaged bubble-bubble drag forces we assume:

$$\bar{F}_{bb}^i = f_Y + f_{bb} [(\eta/\sigma)(v^i - v^{i-1})]^\beta, \quad (8)$$

$$\bar{F}_{bb}^{i+1} = f_Y + f_{bb} [(\eta/\sigma)(v^{i+1} - v^i)]^\beta. \quad (9)$$

Here  $f_{bw}$  and  $f_{bb}$  are material parameters with dimension of force, which will be measured by rheometry in section IV below. Finally,  $f_Y$  represents a yield force in the inter-bubble drag, to remain consistent with rheometrical data presented later on and to reflect the elastic barrier bubbles have to overcome before they slide past each other. Note that the velocities  $v^i$  denote the *averaged* velocities in the  $x$ -direction — the crucial assumption is that the relation between the averaged drag forces and the averaged velocities is simple and can be expressed by a single power law.

We do not know if and how the conjectured forms for the averaged forces can be derived from the non-averaged forces Eqs. (4) and (5) since due to the intermittent and disordered bubble motion, the instantaneous bubble velocities are fluctuating and not necessarily pointing in the  $x$ -direction. For example, there is no a priori reason for the exponents  $\zeta$  and  $\beta$  to be equal and in fact our data strongly indicate that they are not. The best justification for Eqs. (7-9) is a posteriori — the resulting model describes the data well. Note that the bars in

Eqs. (7-9) express an average over disorder, in the sense that these quantities are measured in highly disordered, intermittent flows.

Inserting the expressions from Eqs. (7-9) into Eq. (6) and defining  $k = f_{bw}/f_{bb}$  we arrive at:

$$k \left( \frac{\eta v^i}{\sigma} \right)^{2/3} = \left( \frac{\eta}{\sigma} \right)^\beta [(v^{i+1} - v^i)^\beta - (v^i - v^{i-1})^\beta] . \quad (10)$$

Note that the yield drag contributions  $f_Y$  cancel, which is a particular advantage of the linear geometry we work in. The model predicts flow profiles for arbitrary width and driving rate, once the parameters  $\beta$  and  $k$  are fixed.

### C. Fits

#### 1. Procedure

We compare all 18 runs to solutions of the model. We focus on the central part of the data where  $|v| < 3/4v_0$  to avoid the edge effects near the shearing wheels (for instance the bumps in the low-velocity profiles in Fig. 4(a) and the slip with respect to the wheel in the fast runs). We numerically integrate Eq. (10) from  $y = 0$ , where  $v = 0$ , to the  $y$  value for which  $v = 3/4 \cdot v_0$ , while keeping  $\beta$  and  $k$  fixed. The drag force balance should govern the shape of the velocity profiles for all driving rates and gap widths. Therefore we determine for fixed  $\beta$  the  $k$  values that fit the flow profiles best. The  $k$  values exhibit a systematic variation that depends on the value of  $\beta$ . We quantify this variation by computing the relative variance  $\sqrt{(\delta k^2)/k^2}$  and by repeating the procedure for a range of  $\beta$ , we obtain a plot of the variance as a function of  $\beta$ , see Fig. 4(f). From this graph, we determine the value for which the variance is minimized as  $\beta = 0.36 \pm 0.05$ .

#### 2. Results

Fixing now  $k = 3.75$  and  $\beta = 0.36$ , we capture the shape of all data sets with high accuracy. The resulting model profiles are plotted in Fig. 4(a-c), and we see that for these values all velocity profiles are adequately fitted except for the slowest runs at  $W = 5$  cm. We attribute these deviations for small  $W$  to the observation that edge effects extend further into the shearing region for small gaps.

Note that the model profiles exhibit linear tails, see Fig. 4(e), and that the experimental velocity profiles exhibit approximately the same behavior. We conclude that both the experimental and model profiles do not decay exponentially, in contrast with results found in previous studies [15, 18].

### D. Continuum Limit

The continuum limit of Eq. (10) can be written as:

$$f_{bw} \left( \frac{\eta v}{\sigma} \right)^{2/3} \langle d \rangle^{-1} = \frac{\partial \tau}{\partial y} , \quad (11)$$

$$\tau = \tau_Y + f_{bb} \left( \frac{\eta \langle d \rangle \dot{\gamma}}{\sigma} \right)^\beta , \quad \beta = 0.36 . \quad (12)$$

Hence, the top plate drag can be considered as a body force and the inter-bubble drag force as the divergence of a shear stress  $\tau$ , where  $\tau_Y$  is an undetermined yield stress. Eq. 12 is the constitutive equation for a Herschel-Bulkley fluid [51], and we can now associate the averaged bubble drag force scaling at the local level with the power law scaling of the viscous stress in the Herschel-Bulkley model.

Note that  $\beta = 0.36$  is similar to the power law index  $n = 0.40$  found for the bulk rheology of three-dimensional mobile foams [3, 13] and to the values  $n = 0.33$  and  $n = 0.45$  found for two dimensional bubble rafts in a Taylor-Couette geometry in [16].

The fact that the yield stress does not play a role for our velocity profiles can now be understood in two ways: at the continuum level, since it is a constant it vanishes after taking the divergence of the shear stress, at the bubble level, even though we include a yield force in Eqs. (7-8), the contributions from both neighboring lanes cancel in Eq. (10). Finally, notice that the continuum equations can easily be solved in terms of hypergeometric functions [52].

## IV. RHEOMETRICAL DETERMINATION OF VISCOUS FORCES IN TWO-DIMENSIONAL FOAMS

In this section we will investigate the viscous forces that act at the bubble scale by rheometry, to test and validate the assumptions for the scaling of the bubble-wall drag and the viscous friction inside the foam expressed in Eqs. (4-5). We use an Anton Paar DSR 301 stress controlled rheometer, which can also operate in strain controlled mode. We use the rheometer in strain controlled mode to investigate  $F_{bw}$ . Moreover, we compare measurements, which reflect the actual drag force at the single bubble level ( $F_{bb}$ ), with measurements of the averaged viscous drag force on a bubble in a disordered flow of foam ( $\bar{F}_{bb}$ ).

### A. Bubble-wall drag

We directly measure the bubble-wall friction for foam bubbles produced from the soap solution presented above, with a method that was introduced in [13]. We load a monolayer of bubbles between two PMMA plates

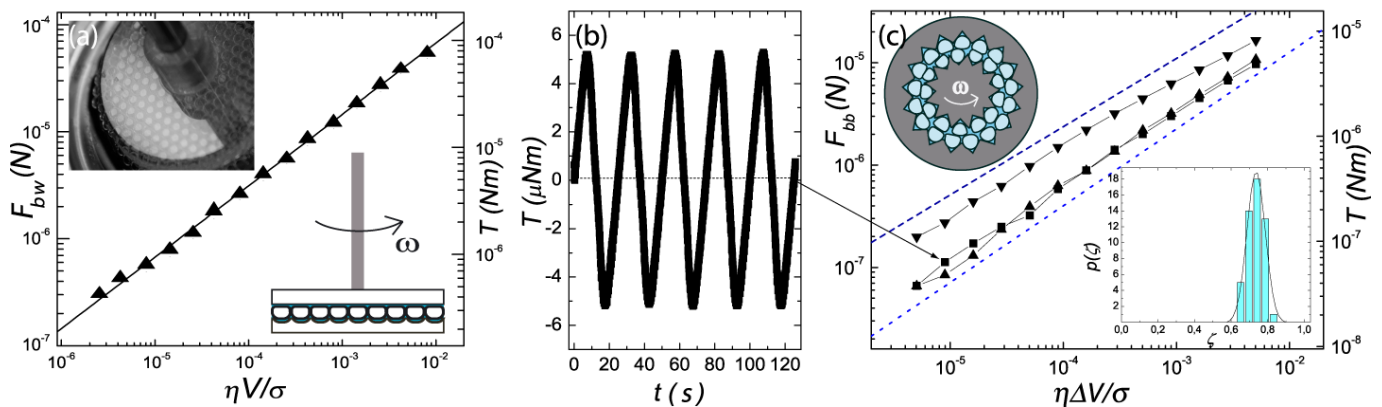


FIG. 6: (Color online) (a) Drag force per bubble exerted on smooth rotated plate as a function of  $Ca$ , probed by the total drag force of a pinned layer of bubbles on a rotating top plate. The solid line represents  $F_{bw} = 0.0015 \pm 0.0001 \cdot (\eta v / \sigma)^{2/3}$ . The upper inset shows a close-up photograph of the rheometrical tool used to measure the bubble-wall drag: the reflection of the flattened facets of radius  $r_c$  used to extract  $R_0$  can be seen clearly. The lower inset shows a side view of the experimental geometry. (b) Raw torque for ordered and commensurate lanes of bubbles sliding past each other. Notice the huge fluctuations with respect to the mean indicated by the horizontal line. The average of the raw data corresponds to the data point in (c) indicated by the arrow. (c) Torque averaged over an integer number of rearrangements as a function of  $\Delta Ca$  for the commensurate case (40 bubbles on inner wheel, 40 bubbles on outer wheel) (■), incommensurate case 41/40 (▼), incommensurate case 44/40 (▲). Dashed lines indicate  $\zeta = 0.67$  resp.  $\zeta = 0.75$ . Upper inset shows a schematic picture of the rheometrical geometry, lower inset shows a histogram of the extracted values of the exponent  $\zeta$ . The width of the bin indicates the error in  $\zeta$ .

of radius  $R_P = 2$  cm. The bubbles are pinned to the lower plate by means of a hexagonal pattern of indentations of size  $\mathcal{O}(d)$ , and can slip with respect to the smooth upper plate which is connected to the rheometer head, see lower inset of Fig. 6(a). We measure the torque  $T$  exerted by the bubbles as a function of the angular velocity  $\omega$  of the smooth plate.

We convert  $T(\omega)$  to  $F_{bw}(Ca)$  in the following way: each bubble exerts a wall stress  $\tau_w = F_{bw} / \pi R_0^2$  on the smooth plate. We integrate the contribution to the torque of this wall stress over the plate:

$$T = \int_0^{R_P} \tau_w r 2\pi r dr = \int_0^{R_P} \frac{F_{bw}}{R_0^2} 2r^2 dr. \quad (13)$$

If we now assume that  $F_{bw} \propto [Ca]^\alpha = \left[\frac{\eta \omega r}{\sigma}\right]^\alpha$ , we can immediately read off from the data that  $\alpha = 0.67$ , see Fig. 6(a), so inserting this expression in the integral Eq. (13) yields:

$$T = \frac{2F_{bw}R_p^{3.67}}{3.67R_0^2}. \quad (14)$$

Since the bubbles are flattened during the measurement, we can only measure  $R_0$  through the flattened facet  $r_c$  by looking at the reflection of the deformed facet, see the upper inset of Fig. 6(a). We find  $r_c = 1.59 \pm 0.05$  mm. As the bubble radius is smaller than  $\kappa^{-1}$  we can express  $R_0$  in terms of  $r_c$  through  $R_0^2 = \sqrt{\frac{3}{2}} r_c \kappa^{-1}$  [48]. Note that this derivation of  $r_c$  in terms of  $R_0$  hinges on the assumption that the bubbles are not too deformed, which is not obvious in the rheometrical geometry, but for lack

of a more precise relation we use it. We finally rescale the horizontal axis by multiplying  $\omega$  with  $\eta R_p / \sigma$ . The resulting curve is plotted in Fig. 6(a): over our measurement range (more than three decades)  $F_{bw} \propto [Ca]^{2/3}$ .

## B. Bubble-bubble drag

### 1. Drag at the bubble scale

To measure the power law scaling of the inter-bubble drag we measure the torque exerted by a foam driven at a strain rate  $\dot{\gamma}$  in a cylindrical Couette geometry, which consists of an inner driving wheel, connected to the rheometer head, rotating inside an outer ring. The rheometrical experiments are performed with bubble rafts, i.e. foams that are not confined by a top plate, as the additional stresses due to the wall would disturb a clean rheological measurement.

Both boundaries are grooved to ensure a no slip boundary for the bubbles, of which a monolayer floats in the shearing region. We start with measuring  $\bar{F}_{bb}$  for the ordered case by keeping the gap between the cylinders such that exactly two layers of bubbles fit in, see the upper inset of Fig. 6(c). The inner radius ( $r_i$ ) is 2.5 cm and the outer radius ( $r_o$ ) is 3.0 cm. We deposit bubbles of 2.2 mm diameter in the grooves, make sure that all bubbles are strictly pinned and remain in their groove, and vary the rotation rate  $\omega$  of the inner cylinder over 3 decades while measuring the torque averaged over an integer number of rearrangement events, see Fig. 6(c).

We multiply  $\omega$  by  $\eta r_i / \sigma$  to rescale the dimensionless



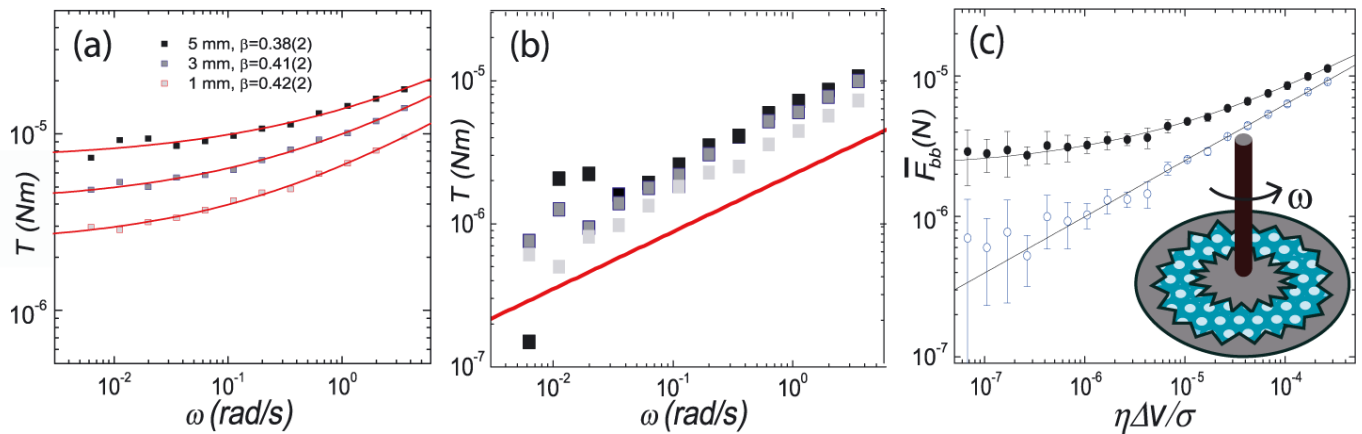


FIG. 7: (Color online) (a) Torque exerted on the inner wheel by a *monodisperse* foam in a Taylor-Couette geometry with  $r_i = 25$ mm,  $r_o = 70$ mm, for different bubble sizes as indicated. Fits are to a Herschel-Bulkley model, and power law indices  $\beta$  from these fits are shown in the graph as well. Surprisingly, the yield stress increases with increasing bubble size — see text. (b) Same data as in (a) with the yield torque from the fit subtracted. The solid line is a power law with index 0.4. (c) Averaged drag force per bubble in a *bidisperse*, disordered foam. The foam is sheared in a Couette cell of inner radius 5 cm, outer radius 7 cm (hence a gap of 9 bubble diameters) without a top plate, see inset. We obtain  $\bar{F}_{bb} = f_Y + f_{bb}(\Delta Ca)^\beta$ , with the yield threshold  $f_Y \approx 2.2 \pm 0.5 \times 10^{-6}$  N,  $f_{bb} \approx 2.5 \pm 0.9 \times 10^{-4}$  N and  $\beta = 0.40 \pm 0.02$  (solid line). Open circles are the same data with the yield torque obtained from the fit subtracted, which are well fit by a pure power-law with exponent 0.4 (dashed line).

velocity difference and we divide the torque by  $r_i$  and the number of bubbles pinned at the inner wheel (e.g. 40) to obtain the averaged bubble-bubble drag force per bubble in the ordered case.

We use three different inner wheels: one with 40 grooves, a second with 41 grooves and a third with 44 grooves. Since the number of grooves in the outer ring is fixed at 40, this allows us to investigate the differences between commensurate and incommensurate numbers of bubbles in the grooves.

For the commensurate case, the result is plotted in Fig. 6(b): All bubbles rearrange simultaneously and thus the signal reflects the torque exerted on a single bubble, amplified by a factor of 40. The elastic barrier that bubbles have to cross before rearranging is clearly visible in the signal. As a result, the torque oscillates tremendously. Nevertheless, the force per bubble averaged over many such events scales with the dimensionless velocity difference as a power law with index 0.7, see Fig. 6 (c). This value is remarkably close to the exponent found for the bubble-wall drag. For these ordered lanes, no signs of a yield plateau are observed in the time averaged signal, and we believe this is due to the fact that all elastic energy that is stored in the bubble deformation is released after yielding, so that one measures purely the viscous drag.

For the incommensurate runs, the raw signal looks more complex, as rearrangements do not occur simultaneously for all 41 or 44 bubbles. The resulting power-law exponents for the averaged drag forces are, however, close to the one observed for the commensurate case. In fact, if we repeat the measurements for both commensurate and incommensurate bubble numbers a multitude of times and fit  $Ca^\zeta$  to the averaged  $F_{bb}$ , we find a distribution

of  $\zeta$ -values around  $\zeta = 0.73$ , see lower inset of Fig. 6(c). The binsize is similar to the errorbar on each individual measurement.

## 2. From local to bulk viscous drag

We observe that the scaling exponent for the viscous drag at the bubble scale,  $\zeta$ , differs markedly from the scaling exponent  $\beta$  of the drag forces inside the bulk foam as extracted from the velocity profiles, e.g.,  $\zeta \approx 0.70$  vs.  $\beta = 0.36$ . We hypothesize this is due to the disordered flow in the foam and will provide rheological evidence in what follows.

To perform rheological measurements of the drag forces, we employ a Couette cell which has an outer ring of radius  $r_o = 7$  cm, such that more layers of bubbles can fit inside the cell. We first will perform measurements on disordered packings of monodisperse bubbles of three different sizes (1, 3 or 5 mm). We observe that the foam deviates substantially from hexagonal packing during flow because the inner radius  $r_i = 2.5$  cm is small, and the curvature is large. We thus induce disorder through geometry.

The resulting measurements show clear yield stress behavior and can be excellently fit by the Herschel-Bulkley model, yielding for all bubble sizes  $\beta \approx 0.4$ , which is markedly lower than the 0.70 found for the drag force in ordered lanes above, and close to the 0.36 extracted from the velocity profiles (see Fig. 7a-b). The observed stress plateau at low strain rates increases with increasing bubble radius, contrary to the intuition that the yield stress is set by the Laplace pressure and should hence scale inversely to the bubble radius. We tentatively attribute

this to the deformation of the bubbles through capillary effects, which are larger for larger bubbles and hence lead to a relatively larger contact size between the bubbles.

In order to further establish a connection between the rheometrical data and the model, we now turn to a geometry with a large inner wheel to increase the measured signal ( $r_i = 5$  cm and  $r_o = 7$  cm), and measure the torque exerted on the inner wheel by a *bidisperse* foam with the same bubble sizes as in the linear shear experiment. We obtain a clear confirmation that indeed the disorder changes the power law scaling of  $\bar{F}_{bb}$ : we again reproducibly measure Herschel-Bulkley behavior with power law index  $\beta \approx 0.40$ , as can be seen in Figs. 7(c).

To convert torques to  $\bar{F}_{bb}$ , we divide the torque by the number of bubbles and  $r_i$ . Since our outer rough boundary forces the bubble velocity to zero, we can rescale the angular frequency to the dimensionless velocity difference  $\eta\Delta v/\sigma$  by assuming a linear velocity profile across the gap, decaying from  $\omega r_i$  to 0. The gap width is approximately  $9\langle d \rangle$  and hence we can estimate  $\Delta v$ . We extract from the rheological measurements an estimate for the ratio  $k = f_{bw}/f_{bb} \approx 5.5 \pm 0.5$ . This is remarkably close to the value  $k = 3.75 \pm 0.5$  extracted from the velocity profiles, given the crude estimates used in converting torques to bubble-bubble drag forces in the rheometrical data — we have oversimplified the shape of the velocity profile in the disordered Couette rheometry, which is neither linear, nor rate independent.

### C. Interpretation

The drag forces exerted on the bubbles by the top plate, which at first sight might be seen as obscuring the bulk rheology of the foam, enable us to back out the effective inter-bubble drag forces and constitutive relation of foams from the average velocity profiles. To further appreciate this fact, note that our model yields linear velocity profiles regardless of the exponent  $\beta$  if the body force due to the wall drag is zero. This is consistent with earlier measurements by Wang et al. [18], where essentially linear flow profiles were found for bubble rafts, i.e., in absence of a top plate.

By comparing the results obtained from the velocity profiles with the rheometrical measurements, we note a remarkable difference between the scaling of the bubble-bubble drag forces at the bubble level, which we have mimicked by strictly ordered bubble rheology, and the scaling of the averaged forces at the bulk level, which we have extracted from the velocity profiles and confirmed by rheometry: we find  $F_{bb} \sim (\Delta v)^{0.70}$  at the bubble level and  $\bar{F}_{bb} \sim (\Delta v)^{0.36}$  at the bulk level.

We speculate that this is closely connected to the non-affine behavior of the bubbles [5, 35, 44]: close to the jamming transition, the effective viscosity of the foam becomes anomalously large due to the fact that bubble motion is much more complicated than if the bubble motion would have been affine, i.e., where the bubbles follow

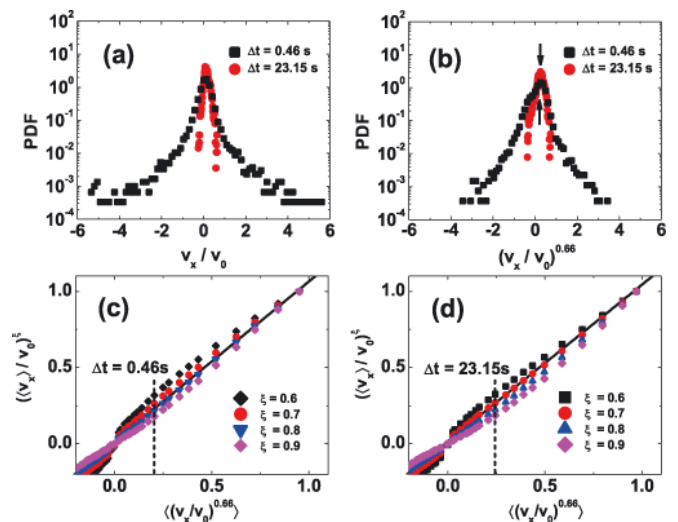


FIG. 8: (Color online) Dimensionless velocity distributions measured for  $W = 7$  cm,  $v_0 = 0.25$  mm/s, and for a  $y$ -position 19 mm away from the center of the gap. Here the averaged velocity equals  $3.1 \times 10^{-2}$  mm/s and the local strain rate equals  $5.6 \times 10^{-3}$  s $^{-1}$ . (a) Distribution of  $v_x/v_0$  for a short time interval ( $\Delta t = 0.46$  s, black squares) and longer time interval ( $\Delta t = 23.15$  s, red circles). For the averages of the dimensionless velocity distributions we find  $\langle v_x/v_0 \rangle \approx 0.125$ , independent of the time averaging interval. (b) Distribution of  $(v_x/v_0)^{2/3}$  for a short time interval ( $\Delta t = 0.46$  s, black) and longer time interval ( $\Delta t = 23.15$  s, red). The averages of the scaled dimensionless velocity distributions equal  $\langle (v_x/v_0)^{2/3} \rangle_{0.46s} \approx 0.205$  and  $\langle (v_x/v_0)^{2/3} \rangle_{23.15s} = 0.245$ . The significance of this is that  $\langle v_x/v_0 \rangle^{2/3} \approx 0.248$ , which is significantly better approximated by the longer time average. (c) Comparison of  $\langle v_x/v_0 \rangle^\xi$  and  $\langle v_x/v_0 \rangle^{2/3}$  along the flow profile for  $\Delta t = 0.46$  s, and for four values of  $\xi$  as indicated. The best linear relation is obtained for  $\xi \approx 0.80$ . Dotted vertical line indicates the averages shown in panel (b). (d) Same as (c), now for  $\Delta t = 23.15$  s. The best linear relation is obtained for  $\xi \approx 0.72$ .

the imposed shear [35]. This picture is corroborated by recent simulations on the bubble model [5], where one recovers this “renormalization” of the drag force exponent [40, 42, 43]. The precise microscopic mechanism, though, is far from understood.

One may wonder why the modification of the exponent of the drag force law is strong for the inter-bubble forces but weak or essentially absent for the bubble wall drag forces. We have no definite answer, although we are fairly confident that the bubble-wall drag forces indeed are not modified. We base this assertion on explorations of the bubble trajectories, described below.

If we assume the Bretherton expression, Eq. (4), to be the correct expression that gives the instantaneous bubble-wall drag force as a function of the instantaneous bubble velocity, our claim is that the averaged bubble-wall drag forces scale similar to the individual bubble-

wall drag force:

$$\langle (\bar{v}/|v|)_x |v|^{2/3} \rangle \approx \langle v_x \rangle^{2/3}. \quad (15)$$

Hence we claim that the time averaged bubble wall drag force is proportional to  $\langle v_x \rangle^{2/3}$ , which is the expression we employ in our model to estimate  $\bar{F}_{bw}$ . In other words, we can interchange the order of taking time averages and “raising to the power  $2/3$ ”.

To check this, we have performed accurate bubble tracking and calculated and compared  $\langle F_{bx} \rangle \equiv \langle (\bar{v}/|v|)_x |v|^{2/3} \rangle$  and  $\langle v_x \rangle^{2/3}$  [36, 53]. In Fig. 8a-b we show examples of distributions of both  $\langle F_{bx} \rangle$  and  $\langle v_x \rangle^{2/3}$ , based on short and long time velocity estimates at a fixed position in the cell. For long times these distributions are narrower and have less weight around zero. For the examples shown in Fig. 8a-b, the averages of the dimensionless velocity distributions equal  $\langle v_x/v_0 \rangle \approx 0.125$ , independent of the time averaging interval. Hence,  $\langle v_x/v_0 \rangle^{2/3} \approx 0.248$ . The averages of the distributions of  $(v_x/v_0)^{2/3}$ , taken over different time intervals, depend now on this time interval and approximate  $\langle v_x/v_0 \rangle^{2/3} \approx 0.248$  better the longer the time interval is: we find  $\langle (v_x/v_0)^{2/3} \rangle_{0.46s} \approx 0.205$  while  $\langle (v_x/v_0)^{2/3} \rangle_{23.15s} = 0.245$ . Since the drag force model deals with (long) time averages, the improvement of the agreement with time is encouraging.

The connection between  $\langle F_{bx} \rangle$  and  $\langle v_x \rangle^{2/3}$  can be probed in more detail by plotting  $\langle F_{bx} \rangle$  as function  $\langle v_x \rangle^\xi$  for a range of strain rates, and estimating for which value of  $\xi$  these two quantities are proportional. The data in Fig. 8c shows that for short times, a value of  $\xi \approx 0.80$ , significantly different from  $2/3$ , leads to the best correlation, while for longer times — 8(d) —, the best value is  $\xi \approx 0.72$ . Therefore, the longer the time interval, the closer  $\xi$  approaches  $2/3$ . The underlying reason is that for increasing time intervals, the distribution of  $v_x/v_0$  becomes narrower and narrower and peaked away from zero, and thus we indeed can interchange the order of taking time averages and “raising to the power  $2/3$ ”.

The bubble-bubble drag forces, on the other hand, involve velocity *differences*, and even at long times we expect their probability distribution to have significant weight around  $\Delta v = 0$ . The situation is then qualitatively similar to that shown in Fig. 8 for short times, and a change from local to global exponent appears reasonable. Unfortunately, testing this explicitly in our data for the bubble trajectories has proven to be prohibitively difficult, not only because velocity differences are smaller and more noisy than velocities, but also since bubble contacts are very hard to establish unambiguously. The precise mechanism responsible for the “renormalization” that leads to the exponent  $\beta \approx 0.4$  remains therefore open.

Finally, the origin of the edge effects that prevent us from fitting our full experimental curves with the model profiles, might be due to the fluid drag near the wheels that was discussed in section II C. Alternatively the origin might lie in the absence of a local flow rule near the driving wheels as reported in [54]. One way to resolve this

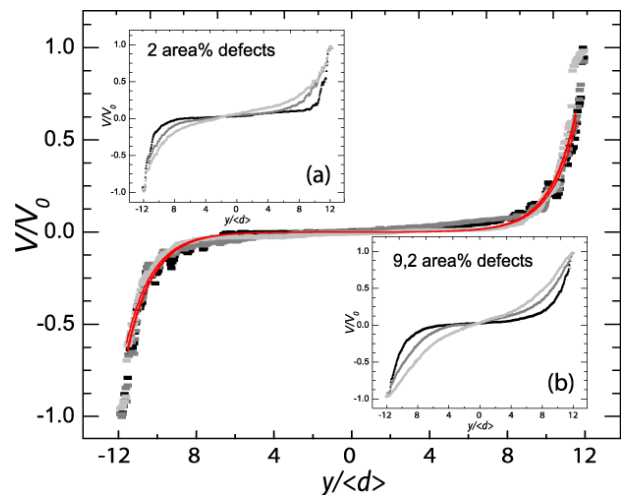


FIG. 9: (Color online) (a) Velocity profiles for a monodisperse, ordered foam with the crystal axis aligned with the wheels. Gap  $W = 7$  cm and  $v_0 = 0.083$  (black),  $0.26$  (dark grey) and  $0.83$  (light grey) mm/s. Solid curves indicate fits to the model Eq. (10) with  $k = 0.3$ ,  $\beta = 2/3$ . (a-b) Velocity profiles for an ordered foam consisting of  $2.7$  mm bubbles for same driving velocities as main panel, to which defects are added in the form of an increasing area fraction of  $1.8$  mm bubbles as indicated.

is accommodating non-local behavior in our model, for instance by incorporating drag terms due to next nearest lanes, similar to the cooperativity length introduced in [54]. We have not pursued this avenue.

## V. ORDERED FOAMS

We have postulated that the disordered bubble motion underlies the anomalous relation between the local bubble-bubble drag forces and the global viscous stresses. To corroborate this conjecture, we shear ordered, monodisperse foams in the linear geometry, similar to what was done in [18]. In this case the bubbles are expected to move affinely with the global shear, in which case one would expect the global viscous drag forces to scale the same as the local ones.

We shear a monodisperse, ordered foam with bubbles of size  $2.7$  mm, produced by blowing nitrogen through one syringe needle at fixed flow rate, at a gap  $W$  of  $7$  cm at  $v_0 = 0.083, 0.26$  and  $0.83$  mm/s. We recover the rate independent and strongly shear banded velocity profiles reported in [18] (see Fig. 9). As in the case of the bidisperse foams, we fit model profiles to our experimental data. For our model to yield rate independent velocity profiles, the drag forces need to balance in the same ratio for all driving velocities. This can only be achieved if  $\beta = 2/3$  since we have already confirmed with rheometry that the exponent governing bubble-wall drag is  $2/3$ . Indeed we find that the experimental profiles are best fit by model profiles if one fixes  $k = 0.3$  and  $\beta = 0.67 \pm 0.05$

[55], see Fig. 9.

### A. Disorder

In our experiment, the complex bubble motion is closely connected to the anomalous scaling of the bubble-bubble drag force, which in turn is reflected in the observed rate dependence of the velocity profiles. We can thus investigate for which levels of disorder the rate dependence of the velocity profiles occurs by gradually increasing the disorder, starting from a monodisperse foam.

To this end we record velocity profiles in a monodisperse foam made of 2.7 mm size bubbles in which we gradually increase the area fraction of smaller (1.8 mm) bubbles. After mixing the two species we measure velocity profiles at  $v_0 = 0.083, 0.26$  and  $0.83$  mm/s. We already observe the occurrence of rate dependent velocity profiles for small quantities of defects, see inset (a) and (b) of Fig. 9, and by visual inspection, we already see the swirling patterns, typical of our 41/59 bidisperse foam, occurring at 2 % disorder. These findings indicate that rate independent flows are in fact limited to a narrow region close to the almost singular case of completely ordered foams.

## VI. ROLE OF THE PACKING FRACTION

In this section we will discuss linear shear experiments where we will vary both the packing fraction (or *wetness*) of our foam  $\phi$  as well as the applied strain rate, to investigate the flow behavior of these foams as a function of density. In particular, we will closely approach the jamming transition, located at  $\phi_c \approx 0.84$ . This allows us to test our drag force balance model over a wide range of experimental situations. Our main findings are that, first, the scaling exponent  $\beta$  appears to be independent of  $\phi$ , and second, that the pre-factor  $k$  is our model (Eq. 10) varies as  $1/(\phi - \phi_c)$  where  $\phi_c \approx 0.84$ .

### A. Varying and measuring $\phi$

In order to vary  $\phi$ , we vary the vertical gap between the glass plates and the bulk solution between 3 and 0.2 mm. We do this by adding or retracting fluid from the reservoir. For large gaps the bubbles get stretched in the vertical direction, and share large deformed facets — the foam effectively becomes dry. For small gaps the bubbles acquire a pancake-like shape, close to purely disc like in the horizontal plane, with only small facets between neighboring bubbles — the foam effectively becomes wet.

To create a homogeneous gap between the liquid surface and the glass plate, we place additional supports under the glass plate to prevent sagging of the top plate during the runs. We monitor the gap width with a Mi-

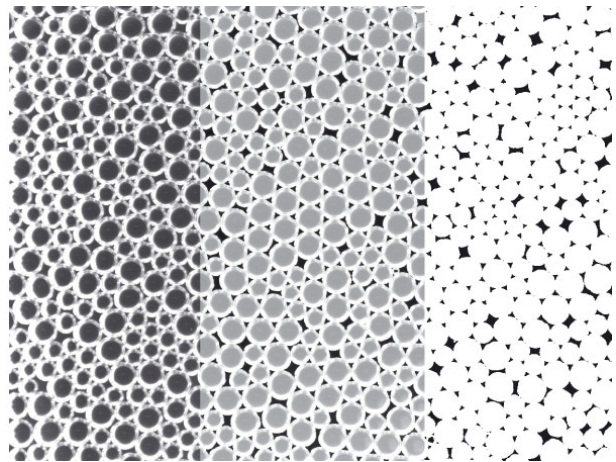


FIG. 10: Image manipulations leading to a definition of  $\phi$ . Left: Raw image. Center: Raw image with reconstructed bubble areas superposed. Note the good agreement. Right: Final binarized image from which packing fraction is deduced.

tutoyo digital depth gauge. If the gap becomes smaller than 0.2 mm the bubbles unjam [56, 57].

We find that in the linear shear cell the accessible range in  $\phi$  is  $0.86 \lesssim \phi \lesssim 0.97$ . If we stay between these limits the system we study is jammed and quasi two-dimensional. It should be noted that for the runs performed at fixed wetness, discussed in the previous sections, we find  $\phi = 0.965 \pm 0.005$ , in reasonable agreement with previous reports on the maximum  $\phi$  that can be obtained in our type of setup [58].

Determining the liquid fraction is not trivial, since various horizontal cuts through the bubble layer will yield different values [59]. We choose our lighting of the bubbles such that the contacts between adjacent bubbles are optimally resolved. We then extract  $\phi$  through image analysis, as illustrated in Fig. 10. We first binarize the images, after which both the bubble centers and the interstices appear bright. We remove the interstices by morphological operations. We then invert the binarized image and fill up the remaining bubble contours. We have checked that the resulting bright disc optimally matches the original bubble contour, see Fig. 10. We then calculate the ratio of white pixels over the total number of pixels and hence obtain a reasonable estimate of  $\phi$ .

Now that we have obtained good estimates of the packing fraction  $\phi$ , we can probe the role of the wetness in setting the flow. We first, in section VIB, briefly discuss a local probe of the non-affine motion, which shows that the bubble motion becomes increasingly non-affine when the wetness is increased. We then investigate the variation of the flow behavior with  $\phi$ , using our model Eq. (10). We first establish, in section VIC, that the exponent  $\beta$  does not vary with  $\phi$  — surprising, give the varying degree of non-affinity. We then find, in section VID, that the force pre-factor  $k$  varies strongly with  $\phi$  and vanishes at  $\phi_c \approx 0.84$  as  $1/(\phi - \phi_c)$ .

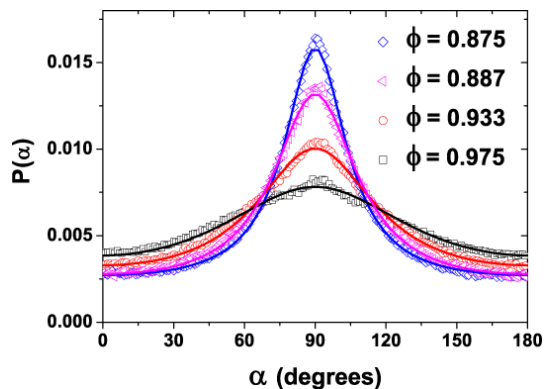


FIG. 11: (Color online) Displacement angle distributions  $P(\alpha)$  for runs for which  $v_0 = 0.26$  mm/s,  $W = 5$  cm and  $\Delta t = 0.46$  s averaged over the shear banded region ( $0 < y < W/3$  and  $2W/3 < y < W$ ) for the range of packing fractions as indicated.

### B. A local measure of the non-affine bubble motion: $P(\alpha)$

A crucial feature of deformations found in simulations of packings of frictionless discs near jamming is the strongly non-affine nature of the particle (bubble) motion [5, 35, 37, 44]. Recently, a simple local probe of this affinity was introduced by Ellenbroek *et al.* who performed simulations of soft frictionless discs [44]. Defining the displacements of contacting particles  $i$  and  $j$  as  $\vec{u}_i$  and  $\vec{u}_j$ , and the vector that connects the centers of particles  $i$  and  $j$  as  $\vec{r}_{ij}$ , the relative displacement angle  $\alpha$  was defined as the angle between  $\vec{r}_{ij}$  and  $\vec{u}_i - \vec{u}_j$ . In other words,  $\alpha = 0^\circ$  corresponds to particles moving away from each other,  $\alpha = 180^\circ$  corresponds to particles moving closer, and  $\alpha = 90^\circ$  corresponds to particles sliding past one another.

The probability distribution  $P(\alpha)$  was found, for shear deformations in particular, to be well fitted by a (periodically extended) Lorentzian peaked around  $90^\circ$  [44, 60]. The width of the peak scales with distance to jamming — at jamming,  $P(\alpha)$  approaches a delta function peaked at  $\alpha = 90^\circ$ .

Of course, in our experiment we have flow, and we cannot determine deformations in linear response. Moreover, our system is not homogeneous. Nevertheless, as a coarse measure of the degree of non-affine bubble motion, which we claim underlies the anomalous scaling exponent  $\beta$  in disordered systems, we have calculated  $P(\alpha)$  focussing on finite time displacement fields ( $v_0 = 0.216$  mm/s,  $W = 5$  cm,  $\Delta t = 0.46$  s).

In Fig. 11 we show  $P(\alpha)$  averaged over the regions  $0 < y < W/3$  and  $2W/3 < y < W$  where most of the flow takes place, and averaged in the  $x$ -direction over 50 mm in the center of the cell. We limit ourselves to this region, because, in particular for the wet runs, there is hardly any flow in the center region of the cell and the

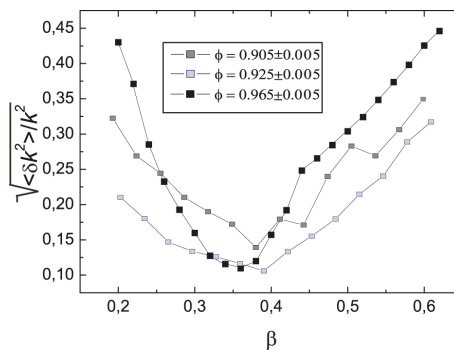


FIG. 12: (a) variance in  $k$  values for all six runs performed at  $\phi = 0.905$  (grey squares) and  $\phi = 0.925$  (light grey squares). The variance at  $\phi = 0.965$  (black squares) is data from Fig. 4(f). A clear minimum can be observed around  $\beta = 0.38$ .

peaks in  $P(\alpha)$  are less pronounced in this region. We find that, analogous to what is found in simulations [44], the distributions become increasingly peaked around  $\alpha = 90^\circ$  for increasing wetness. Moreover, the distributions are well fit by the same Lorentzian fit that also captures the numerical displacement fields well [60].

Hence, this simple measure of non-affine motion strongly indicates that the degree of non-affinity increases for wetter foams. We believe that this is the first experimental measurement of this distribution that shows the proximity of the jamming transition. Detailed studies of the role of the local strain rate or the time interval over which displacements are measured are deferred to later work.

### C. Variation of the exponent $\beta$ with $\phi$

We now investigate the validity of applying the drag force balance model with a fixed  $\beta = 0.36$  for varying  $\phi$ . The microscopic exponent  $2/3$  which governs the flow of a bubble past a wall appears to be independent of the particularities of the foam flow [30, 61]. On the other hand, it is not at all obvious that  $\beta$ , which governs the averaged bubble-bubble drag forces, does not depend on  $\phi$ . As we have seen,  $\beta$  is set by the disorder in the system and the non-affine bubble motion that occurs in conjunction with that, and as we have shown in the previous section, the degree of non-affinity varies substantially with  $\phi$ .

To see if  $\beta$  indeed depends on the foam density we perform two additional scans over the same six shear rates as employed in section III for a bidisperse foam at a gap width  $W = 7$  cm, while first fixing  $\phi = 0.905 \pm 0.005$  and then  $\phi = 0.925 \pm 0.005$ . We look for a minimum of the variance in  $k$  over the six velocity profiles as a function of  $\beta$  (see grey and light grey squares in Fig. 12). We observe that the model fits best to all six runs performed at  $\phi = 0.905$  for  $\alpha = 2/3, \beta = 0.38 \pm 0.05$  (see Fig. 12) and  $k = 7.5$ , whereas the model best matches the runs

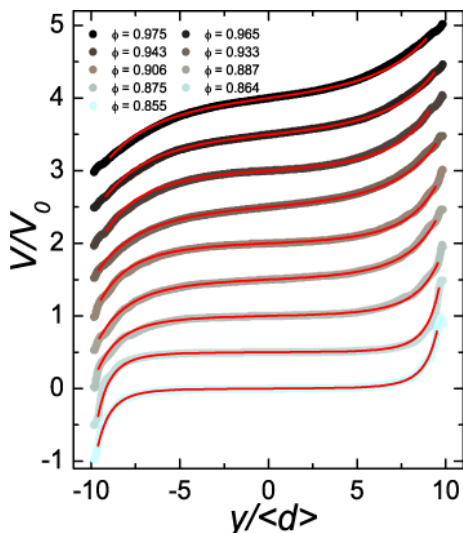


FIG. 13: (Color online) Velocity profiles in linearly sheared foam at fixed driving rate ( $v_0 = 0.26$  mm/s), for  $\phi$  varying between  $0.855 \leq \phi \leq 0.975$  at  $W = 7$  cm. Fits are solutions to linear drag force balance model with  $\alpha = 0.67$  and  $\beta = 0.36$  fixed.  $k$  is extracted from the fits and plotted in Fig. 14 as a function of  $\phi - \phi_c$ .

performed at  $\phi = 0.925$  for  $\alpha = 2/3, \beta = 0.39 \pm 0.05$  (see Fig. 12) and  $k = 5.8$ , thus strongly indicating that within our range of accessible liquid fractions  $\beta$  seems to be constant. For comparison, we include the variance for the runs described in section III B that was plotted in Fig. 4(f). Remarkably,  $\beta$  remains a constant with varying  $\phi$  while the degree of non-affinity varies. While we do not pretend to understand this, we do remark that  $\beta$  and  $P(\alpha)$  essentially encode different routes towards jamming and thus towards increasing non-affinity:  $\beta$  is renormalized by the increasing non-affinity as one lowers the strain rate  $\dot{\gamma}$  towards jamming, while  $P(\alpha)$  monitors non-affinity as a function of density.

#### D. Scaling of the force pre-factor $k$ with $\phi$

Now that we have established that  $\beta$  is independent of  $\phi$ , we will probe the variation of  $k$  with  $\phi$ . We measure averaged velocity profiles at gap widths  $W = 5$  cm and  $W = 7$  cm and fixed  $v_0 = 0.26$  mm/s (the third slowest driving velocity), for packing fractions varying between  $\phi = 0.855$  and  $\phi = 0.975$ . The velocity profiles for  $W = 5$  cm are plotted in Fig. 13, and are seen to become increasingly shear banded as we approach  $\phi_c$  [64]. This trend is reflected in the increase of  $k$  as we approach  $\phi_c$ . We obtain  $k$  by fitting solutions of our drag force balance model with  $\alpha = 0.67$  and  $\beta = 0.36$  to these profiles. The resulting fits are shown as red lines in Fig. 13, and fit the data well.

In Fig. 14 we plot  $k$  as a function of  $\phi - \phi_c$ , with  $\phi_c$

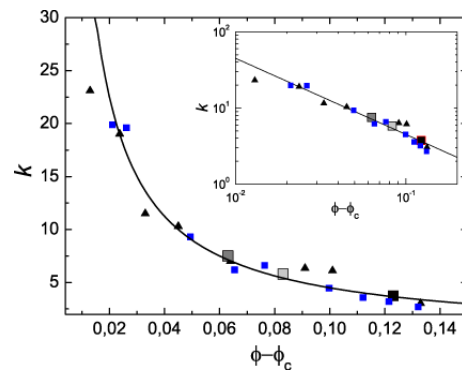


FIG. 14: (Color online) Scaling of  $k$  with  $\Delta\phi \equiv \phi - \phi_c$ . Triangles: data obtained from fits depicted in Fig. 13 where  $W = 5$  cm. Squares: data for gap of 7 cm. Large squares correspond to runs at  $v_0 = 0.26$  mm/s from Fig. 12. Solid line:  $0.45/\Delta\phi$ . Inset: same data on log-log scale.

the theoretically predicted and experimentally measured value of the unjamming packing fraction:  $\phi_c = 0.842$  [40, 62, 63]. In good approximation we obtain that

$$k \propto 1/(\phi - \phi_c) \quad (16)$$

We can tentatively explain the observed scaling of  $k$  with a simple argument based on the sizes of the facets in the foam. At fixed  $\phi$ , our drag force balance model yields a value of  $k$  that sets the relative influence of the bubble-wall drag with respect to the bubble-bubble drag and which we have conjectured to be given by  $k \propto f_{bw}/f_{bb}$ . As we have already discussed,  $f_{bw} \propto \sigma r_c$  with  $r_c$  the radius of the flattened contact between the bubble and the wall and  $f_{bb} \propto \sigma \kappa_c^2$ , with  $\kappa_c$  the radius of the flattened contact between neighboring bubbles. Thus we expect:

$$k \propto r_c/\kappa_c^2. \quad (17)$$

While  $r_c$  is set by the buoyancy and hence does not vary strongly with the gap distance between glass plate and liquid surface — only becoming slightly smaller as the bubbles get stretched at large gaps —  $\kappa_c$  is strongly dependent on the gap size and hence on the packing fraction of the foam.

The size of  $\kappa_c$  should depend on the deformation (also called the overlap)  $\delta\xi$  as [26]:

$$\kappa_c \propto (\delta\xi)^{1/2}. \quad (18)$$

Similar to simulations of two-dimensional frictionless discs [38, 44] we can relate the overlap  $\delta\xi$  to the packing fraction  $\phi$ :

$$\delta\xi \propto \Delta\phi. \quad (19)$$

Simple substitution of this result into Eq. (17) yields

$$k \propto r_c/\kappa_c^2 \propto 1/\delta\xi = 1/(\Delta\phi), \quad (20)$$

which is fully consistent with our experimental results, see the solid line in Fig. 12

Note that in the above we have only focussed on the radius of the deformed facets. A proper analysis would include the size of the Plateau border around the contact, which is where the dissipation also occurs [29, 32]. For instance, in [61] the bubble-wall drag force scales as  $F^{bw} \propto Ca^{0.64} \phi_t^{-0.26}$  and a proper treatment would entail such analysis, even though the functional dependence on the Plateau border size is always weak. Moreover, in all of these works, the functional dependence of the drag force with  $\phi$  is smooth around  $\phi_c$  and hence will not influence the observed scaling around that point.

## VII. DISCUSSION AND CONCLUSION

We have measured velocity profiles in linearly sheared quasi-two-dimensional foams in the liquid-glass configuration. We find that bidisperse, disordered foams exhibit strongly rate dependent and inhomogeneous (shear banded) velocity profiles, while monodisperse, ordered foams are also shear banded, but essentially rate independent. We capture these findings in a simple model that balances the drag forces in our system. The scaling forms for these drag forces are verified by independent rheological measurements. Finally, we apply our model to velocity profiles obtained for foams at varying packing fraction, and measure and describe the scaling of the inverse foam consistency with packing fraction.

This work raises several questions. First, can the

difference between the local bubble-bubble drag force scaling and the global (averaged) bubble-bubble drag force scaling be understood theoretically? This difference in scaling exponents appears similar to the change from local drag forces to global rheological laws, observed in simulations of (variants) of the bubble model [5, 40, 41, 43, 65], but a precise connection is lacking at present. Closely connected, is our scenario an example of a general route by which aspects of the ubiquitous Herschel-Bulkley (power law) rheology observed for a wide range of disordered materials can be rationalized?

Second, how robust are our experimental results? For example, would similar flows in Hele-Shaw cells behave differently, as suggested by the results of Debrégeas [15]? We also wonder if our model is able to capture shear banded flows in Couette geometries, where the curvature plays an important role, in particular since the foam has a finite flow threshold [66]. Third, can similar phenomena and models as described here be extended to three dimensional flows of foams and emulsions — where flows in the latter can be captured by confocal imaging and MRI [27, 54, 67, 68]? Fourth, how should our local models be compared to the non-local effects recently discussed for emulsion flows [54, 67]?

### Acknowledgments

The authors wish to thank Jeroen Mesman for technical assistance. GK kindly acknowledges Nikolai Denkov for illuminating discussions. GK and MM acknowledge support from physics foundation FOM, and MvH acknowledges support from NWO/VIDI.

- 
- [1] R. Höhler and S. Cohen-Addad, *J. Phys. Cond. Matt.* **17**, R1041 (2005).
  - [2] T.G. Mason, J. Bibette and D. A.Weitz, *J. Coll. Interf. Sci.* **179**, 439 (1996); W. Losert *et al.*, *Phys. Rev. Lett.* **85**, 1428, (2000); P. Coussot *et al.*, *Phys. Rev. Lett.* **88**, 218301, (2002); R. Besseling *et al.*, *Phys. Rev.Lett.* **99**, 028301, (2007).
  - [3] L. Bécu, S. Manneville and A. Collin, *Phys. Rev. Lett.* **96**, 108203, (2006).
  - [4] A.M. Kraynik, *Annu. Rev. Fluid. Mech* **20**, 325 (1988).
  - [5] D.J. Durian, *Phys. Rev. Lett.* **75**, 4780 (1995).
  - [6] C. Gilbreth, S. Sullivan and M. Dennin, *Phys. Rev. E* **74**, 051406 (2006).
  - [7] D. Weaire and S. Hutzler, *The Physics of Foams* (Clarendon Press, Oxford, 1999)
  - [8] R.G. Larson, *Structure and Rheology of complex fluids* (Oxford University Press,1998)
  - [9] S.A. Khan, C.A. Schnepper and R.C. Armstrong, *J. Rheology* **32** 69 (1988).
  - [10] H.M. Princen and A.D. Kiss, *J. Colloid Interface Sci.* **128**, 176 (1989).
  - [11] A.D. Gopal and D.J. Durian, *Phys. Rev. Lett.* **91**, 188303 (2003).
  - [12] J. Lauridsen, M. Twardos, and M. Dennin, *Phys. Rev. Lett.* **89**, 098303 (2002).
  - [13] N.D. Denkov, V. Subraminian, D. Gurovich and A. Lips, *Coll. Surf. A* **263**, 129 (2005).
  - [14] G. Katgert, M.E. Möbius and M. van Hecke, *Phys. Rev. Lett.* **101**, 058301 (2008).
  - [15] G. Debrégeas, H. Tabuteau and J.-M. di Meglio, *Phys. Rev. Lett.* **87**, 178305 (2001).
  - [16] J.Lauridsen, G.Chanan and M. Dennin, *Phys. Rev. Lett.* **93**, 018303 (2004).
  - [17] L. Bragg and J.F. Nye, *Proc. R. Soc. Lond. A* **190**, 474 (1947).
  - [18] Y. Wang, K. Krishan and M. Dennin, *Phys. Rev. E* **73** 031401 (2006).
  - [19] C.S. Smith, *Metal Interfaces* American Society for Metals, Cleveland, OH (1952).
  - [20] M.F. Vaz and M.A. Fortes, *J. Phys. Cond. Matt.* **9**, 8921 (1997).
  - [21] B. Dollet, F. Elias, C. Quilliet, C. Raufaste, M. Aubouy and F. Graner, *Phys. Rev. E.* **71**, 031403 (2005).
  - [22] A. Kabla, J. Scheibert and G. Debregeas, *J. Fluid Mech.* **587**, 45 (2007).
  - [23] I. Cheddadi, P. Saramito, C. Raufaste, P. Marmottant and F. Graner, *Eur. Phys. J. E* **27**, 123 (2008).
  - [24] E. Janiaud, D. Weaire and S. Hutzler, *Phys. Rev. Lett.*

- 97**, 038302 (2006).
- [25] T.G. Mason, J. Bibette and D.A. Weitz, *J. Coll. Interf. Sci.* **179**, 439 (1996).
- [26] M.-D. Lacasse, G.S. Grest, D. Levine, T.G. Mason and D.A. Weitz *Phys. Rev. Lett.*, **76**, 3448 (1996).
- [27] J. Brujić, S. F. Edwards, I. Hopkinson, and H. A. Makse, *Physica A.* **327**, 201 (2003).
- [28] S. Zhou, Q. Long, D. Wang and A.D. Dinsmore, *Science* **312**, 1631 (2006).
- [29] N.D. Denkov, S. Tcholakova, K. Golemanov, V. Subramanian and A. Lips, *Coll. Surf. A* **282**, 329 (2006).
- [30] I. Cantat, N. Kern and R. Delannay, *Europhys. Lett.* **65**, 726 (2004).
- [31] A. Saugey, W. Drenckhan and D. Weaire, *Phys. Fluids* **18**, 053101 (2006).
- [32] E. Terriac, J. Etrillard and I. Cantat, *Europhys. Lett.* **74**, 909 (2006).
- [33] N.D. Denkov, S. Tcholakova, K. Golemanov, K.P. Ananthapadmanabhan, and A. Lips, *Phys. Rev. Lett.* **100**, 138301 (2008).
- [34] F.P. Bretherton, J. Fluid Mech.ovich and A. Lips, *Coll. Surf. A* **263**, 129 (2005).
- [35] A.J. Liu, S. Ramaswamy, T.G. Mason, H. Gang and D.A. Weitz, *Phys. Rev. Lett.* **76** 3017, (1996).
- [36] M.E. Mobius, G. Katgert and M. van Hecke, *arXiv/cond-mat.soft:0811.0534*.
- [37] H. A. Makse, N. Gland, D. L. Johnson and L. M. Schwartz, *Phys. Rev. Lett.* **83**, 5070 (1999).
- [38] C.S. O'Hern, L.E. Silbert, A.J. Liu and S.R. Nagel, *Phys. Rev. E* **68**, 011306 (2003).
- [39] W.G. Ellenbroek, Z. Zeravcic, W. van Saarloos and M. van Hecke, *in preparation*.
- [40] P. Olsson and S. Teitel, *Phys. Rev. Lett.* **99**, 178001 (2007).
- [41] T. Hatano, *J. Phys. Soc. Jap.* **77**, 123002 (2008).
- [42] V.J. Langlois, S.Hutzler and D. Weaire, *Phys. Rev. E* **78**, 021401 (2008).
- [43] J. Remmers, E. Woldhuis, B.P. Tighe, M. van Hecke and W. van Saarloos, *in preparation*
- [44] W.G. Ellenbroek, E. Somfai, M. van Hecke and W. van Saarloos, *Phys. Rev. Lett.* **97**, 258001 (2006).
- [45] H. A. Makse, D. L. Johnson and L. M. Schwartz, *Phys. Rev. Lett.* **84**, 4160 (2000).
- [46] J.M. Andreas, E.A. Hauser and W.R. Tucker, *J. Phys. Chem.* **42**, 1001 (1938).
- [47] This is done to ensure the packing fraction remains constant during the strain rate sweep; when the entire circumference of the wheel is covered with bubbles a balance results between bubbles dragged out of the system and injected back in. If we would sweep from slow to fast driving rates, this balance is not achieved, resulting in a packing fraction that decreases during the experiment.
- [48] P. Aussillous and D. Quéré, *Europhys. Lett.* **59**, 370 (2002).
- [49] S.A. Koehler, S. Hilgenfeldt and H.A. Stone, *Phys. Rev. Lett.* **82**, 4232 (1999).
- [50] D.A. Reinelt and A.M. Kraynik, *J. Coll. Interf. Sci.* **132**, 491, (1989).
- [51] W.H. Herschel and R. Bulkley, *Koll. Zeitschrift* **39**, 291 (1926).
- [52] B.P. Tighe, private communications, D. Weaire, S. Hutzler, V.J. Langlois and R.J. Clancy, *Phil. Mag. Lett.* **88**, 387 (2008).
- [53] One subtlety one encounters is that from the tracking we can only estimate the velocity from ratios of displacements and time intervals, and for the experimentally accessible timescales, the statistics of the velocities thus obtained have been found to depend on the time interval — see [36].
- [54] J. Goyon, A. Colin, G. Ovarlez, A. Ajdari and L. Bocquet, *Nature* **454**, 84 (2008).
- [55] The value of  $k$  is remarkably small. If we assume that prefactor  $f_{bw}$  for the bubble wall drag remains unchanged for the ordered foam, this means that the bubble-bubble drag prefactor  $f_{bb}$  is much larger compared to its value for a disordered foam. Note however, that the power law exponent  $\beta$  greatly influences the value of the drag force: for instance, if  $\Delta v = 0.001$  m/s, then  $(\eta v/\sigma)^{2/3} = 1.6 \times 10^{-3}$ , whereas  $(\eta v/\sigma)^{0.36} = 3.1 \times 10^{-2}$ , which is more than an order of magnitude larger.
- [56] S.J. Cox and E. Janiaud, *Phil. Mag. Lett.* **88**, 693 (2008).
- [57] This might be due to the fact that the gap is then of the size of the Plateau borders that connect the flat film between the bubble and the glass plate and the flat film between neighboring bubbles, and hence the latter vanishes. If the gap becomes larger than 3 mm the foam buckles and develops a three dimensional structure.
- [58] C. Raufaste, B. Dollet, S. Cox, Y. Jiang and F. Graner, *Eur. Phys. J. E* **23**, 217 (2007).
- [59] One could try to relate the liquid fraction to the gap between the liquid surface and the glass plate. This distance, however, does not unambiguously set  $\phi$  in our experiment: we observe a large hysteresis effect, i.e., increasing or decreasing the gap to a certain value does not yield the same packing fraction  $\phi$ . This probably due to the open boundary conditions in the horizontal plane. Another measure that has been derived in [58] relates the measured length of the deformed facets of the bubbles just before a T1 event to  $\phi$ . In our experiments, though, it is not clear how the occurrence of T1-events can precisely be defined, since there is no obvious separation of the deformation scales during and outside of a T1-event.
- [60] W.G. Ellenbroek, M. van Hecke and W. van Saarloos, *in preparation*.
- [61] C. Raufaste, *PhD-thesis*, <http://tel.archives-ouvertes.fr/docs/00/19/32/48/PDF/TheseRaufaste.pdf> (2007).
- [62] F. Bolton and D. Weaire, *Phys. Rev. Lett* **65**, 3449 (1990).
- [63] F. Lechenault, O. Dauchot, G.Biroli and J.-P. Bouchaud, *Europhys. Lett.* **83**, 46003 (2008).
- [64] Note that this trend is opposite to what was observed by Debrégeas et al. in [15]: there the authors find that the velocity profiles become less shearbanded with increasing liquid fraction. We cannot explain this result and conclude it to be one of the many open questions surrounding that work.
- [65] N.Xu and C.S. O'Hern, *Phys. Rev. E* **73**, 061303 (2006).
- [66] M. Dennin, *J. Phys. Condens. Matt.* **20**, 283103 (2008).
- [67] G. Ovarlez, S. Rodts, A. Ragouilliaux, P. Coussot, J. Goyon and A. Colin, *Phys. Rev. E* **78**, 036307 (2008).
- [68] S. Rodts, J. C. Baudez and P. Coussot, *Europhys. Lett.* **69**, 636 (2005).